JEE Journal of Ecological Engineering

Journal of Ecological Engineering, 2026, 27(6), 289–311
https://doi.org/10.12911/22998993/217578
ISSN 2299–8993, License CC-BY 4.0

Received: 2025.12.11
Accepted: 2026.04.16
Published: 2026.05.01

Photodegradation of enrofloxacin via coconut fiber-derived hydrochar@OCN composite

Adhi Yuniarto[1*], Urifatus Eka Kurnia Sari[1,2], Ervin Nurhayati[1], Bara Awanda Marhendra[1], Asranudin[3], Muchammad Tamyiz[2]

[1] Department of Environmental Engineering, Faculty of Civil, Planning, and Geo-Engineering, Institut Teknologi Sepuluh Nopember, Kampus ITS Sukolilo, Surabaya, Indonesia
[2] Department of Environmental Engineering, Universitas Nahdatul Ulama Sidoarjo, Sidoarjo, Indonesia
[3] Research Center for Applied Microbiology, National Research and Innovation Agency, Cibinong, Indonesia
* Corresponding author's e-mail: adhy@its.ac.id

ABSTRACT

Enrofloxacin (ENR), a widely used fluoroquinolone antibiotic, has emerged as a persistent environmental contaminant that contributes to the spread of antimicrobial resistance. Photocatalytic degradation offers a promising approach for its removal from aqueous environments. This study aims to evaluate the photocatalytic performance of a composite material based on coconut shell hydrochar@O-doped g-C_3N_4 (hydrochar@OCN) for ENR degradation under various operational and environmental conditions. The effects of water matrices (deionized, rain, river, lake, and spring water), solution pH (2, 4, 7, 10, 12), catalyst dosage (1, 1.5, 2, 2.5, 3 g/L), hydrochar@OCN composition (hydrochar, OCN, 1%, 10%, 20%), and initial ENR concentration (3, 5, 7, 9, 10 mg/L) were systematically investigated. The experiments were conducted for 90 minutes, consisting of a 30-minute dark adsorption stage to reach adsorption equilibrium, followed by 60 minutes of LED irradiation to initiate photocatalytic degradation. The results revealed that ENR removal efficiency strongly depended on the operating parameters in 60 minutes. The deionized water matrix with hydrochar loading of 10% in OCN, and neutral pH (pH 7) yielded the highest removal photocatalytic activity (70.29%). While the lake water reaches 47.48%, river (53.26%), rainwater (61.23%), and spring water (61.23%). The optimal conditions were achieved at a catalyst dosage of 3 g/L, with a degradation efficiency of 94.20%, and at an initial ENR concentration of 3 mg/L, with a degradation efficiency of 94.93%. The photocatalytic degradation followed pseudo-first-order kinetics with a rate constant of k = 0.086 g mg^{-1} min^{-1}, demonstrating the superior activity of the optimized composite.

Keywords: coconut fiber, carbon nitride, enrofloxacin, hydrochar, photocatalytic.

INTRODUCTION

The widespread occurrence of antibiotics in aquatic environments has become a critical global concern due to their persistence, bioaccumulation potential, and the increasing threat of antimicrobial resistance (Symochko et al., 2019). Among various antibiotics, enrofloxacin (ENR), a member of the fluoroquinolone class (Sciscenko et al., 2021), is extensively applied in veterinary medicine, livestock farming, and aquaculture to prevent and treat bacterial infections (Fang et al., 2023). In Indonesia, ENR is used as a livestock medication, and its use has become widespread. ENR residues in chicken meat reached 185.93 µg/kg, while in chicken eggs, they reached 145.32 µg/kg, exceeding the permissible limit of 100 µg/kg (Rohana and Prabhata, 2023). Persistent exposure to ENR can promote the development of antibiotic-resistant bacteria (Symochko et al., 2019), disrupt aquatic microbial balance, and endanger higher organisms through bioaccumulation and biomagnification in the food chain (Bilal et al., 2020).

Conventional wastewater treatment systems are generally ineffective in eliminating ENR because of its high chemical stability and resistance to biodegradation. These limitations have prompted the exploration of advanced oxidation processes, particularly photocatalysis, as a sustainable and efficient strategy for degrading recalcitrant

pharmaceutical pollutants (Mathew et al., 2020). Graphitic carbon nitride (g-C_3N_4) has emerged as a promising metal-free photocatalyst owing to its suitable band gap, low cost, and high stability under visible light irradiation (Wang et al., 2018). Nevertheless, pristine g-C_3N_4 suffers from low photocatalytic efficiency caused by rapid charge recombination and limited surface area. To address these drawbacks, oxygen doping has been introduced to enhance charge separation and visible-light absorption, while coupling g-C_3N_4 with porous carbon materials such as hydrochar further improves surface adsorption and electron transport (Chen et al., 2022).

Despite the growing body of research on photocatalytic degradation using modified g-C_3N_4, studies focusing on the influence of environmental parameters, including water matrix, pH, pollutant concentration, and catalyst dosage, remain limited, especially when using biomass-derived composites. Therefore, investigates the effect of these environmental factors on the photodegradation efficiency of ENR using a coconut husk-based hydrochar@O-doped g-C_3N_4 composite (hydrochar@OCN). Coconut husk, an abundant agricultural byproduct in tropical regions, serves as a sustainable carbon source for hydrochar synthesis, contributing to waste valorization and environmental circularity.

Previous researchers (Xu et al., 2022), have successfully composited g-C_3N_4/sludge biochar with sulfur doping, degrading around 95.07% of tetracycline antibiotics. Wang and Wang (2022), also composite γ-Fe_2O_3/O-gC_3N_4/coconut biochar composite showed superior catalytic activity, in which complete degradation of antibiotic sulfamethoxazole (SMX) was quickly achieved, with the mineralization ratio of 97.5%. The comparison of this research with previous research is presented in Table 1. The novelty of this study lies in the synergistic integration of oxygen-doped g-C_3N_4 and coconut husk-derived hydrochar, which provides a dual-function composite combining strong adsorption capacity with enhanced visible-light photocatalytic activity. Moreover, this work aims to reveal whether hydrochar@OCN can degrade the fluoroquinolone antibiotic ENR, which is widely used in Indonesia for livestock health needs.

MATERIAL AND METHODS

Material

Urea, dicyandiamide, and oxalic acid were purchased in analytical grade and used as precursors for synthesizing O-doped graphitic carbon nitride (OCN). Raw coconut husk biomass was obtained from local agricultural waste in East Java, Indonesia, and utilized as the carbon source for hydrochar (HC) synthesis. Enrofloxacin (ENR, ≥99% purity) served as the model antibiotic pollutant. Deionized (DI) water was used for all solution preparations, while other water matrices, including rain, river, lake, and spring water, were collected locally and filtered before use. Teflon hydrothermal, oven, hotplate, photocatalytic reactor, centrifuge, visible light LED (Blue, 460 nm), total power 60 watts (0.44 mW/cm²), glassware, and micropipettes were used in this research.

Synthesis of oxygen-doped g-C_3N_4 (OCN)

The first step is to weigh 10 g of urea and 5 g of dicyandiamide (2:1) with 10% (total mass) of oxalic acid. After that, they are placed in a crucible and heated at 550 °C for 4 hours with a calcination rate of 2 °C per minute. This process produces

Table 1. Comparison of previous research

No.	Title	Material	Variation	Reference
1.	Magnetic 2D/2D oxygen doped g C_3N_4/biochar composite to activate peroxymonosulfate for degradation of emerging organic pollutants	oxygen doped g C_3N_4/biochar	Dosage (0,4 g/L), time (0-250 minute), and efficiency (97.5%)	Wang and Wang (2022)
2.	Degradation of tetracycline using persulfate activated by a honeycomb structured S doped g- C_3N_4/biochar under visible light	S doped g- C_3N_4/ biochar	Dosage (0.25-1.25 g/L), time (30 minute dark dan 30 minute light), and efficiency (81.4%)	Xu et al., 2022
3.	Hybrid biochar-graphitic carbon nitride (g- C_3N_4) composite photocatalyst: a facile strategy for enhanced degradation of Ciprofloxacin (CIP)	biochar-graphitic carbon nitride (g- C_3N_4)	Dosage (10 ppm), time (30 minute dark and 240 minute light), and efficiency (51%)	Idrees et al., 2025

Note: dosage, reaction time, light conditions, and degradation efficiency are reported as described in the respective references.

a yellow powder (g-C_3N_4), which is then ground. The result is further calcined at 520 °C for 2 hours and produces oxygen-doped g-C_3N_4 (OCN).

Preparation of coconut husk hydrochar

The coconut husk is cut into small pieces, washed thoroughly, and then dried in the sun. Then, it is oven-dried until dry, ground, and then sieved to a 160-mesh size. The sieved coconut husk powder is placed in a teflon hydrothermal filter, and distilled water is added at a ratio of 1:20 (w/v). The teflon hydrothermal filter is heated at 200 °C for 10 hours. After heating, the coconut husk hydrochar is filtered and dried at 110 °C for 3 hours.

Synthesis of hydrochar@O-doped g-C_3N_4 composite

Coconut fiber hydrochar at 1%, 10%, and 20% of the g-C_3N_4 mass. After that, it was placed in a beaker and mixed with 100 mL of distilled water, and stirred for approximately 20 hours. The composite was evaporated at 80 °C until dry (S. Wang and Wang, 2022). After that, it was calcined at 200 °C for 1 hour to form the coconut husk hydrochar@OCN composite.

Preparation of enrofloxacin solution

Enrofloxacin exhibits maximum absorbance at a wavelength of 324 nm (Shen et al., 2019) with an average pH of 3-11 (Jiang et al., 2024). This study utilized a wavelength of 324 nm with a Genesys 150 spectrophotometer, which had a range of 200–400 nm. A calibration curve of the enrofloxacin standard solution with concentrations of 1, 3, 5, 7, 10, 15, 20, 25, 30, 35, 40, 45, and 50 mg/L to obtain a linear regression equation value of $y = 0.0276x - 0.006$ with a correlation coefficient (R^2) of 0.996. Linear regression equations are usually used to express linear relationships between two or more variables.

Photocatalytic degradation experiments

Composite variations (1%, 10%, 20%) were contacted with ENR (3, 5, 7, 9, and 10 mg/L) at pH values (2, 4, 7, 10, 12) using predetermined doses (1, 1.5, 2, 2.5, and 3 g/L) and using water matrices (DI water, lake, rain, river, and spring water) and rotated at 525 rpm. The degradation process began with the first 30 minutes in the dark to maximize adsorption. After 30 minutes, the LED light was turned on, and samples were taken every 10 minutes for up to 1 hour. The samples were centrifuged to precipitate the composites that were also taken. The centrifuged samples were filtered using a 0.2 μm filter, and then their concentration was measured using UV-vis spectroscopy at a wavelength of 324 nm.

RESULTS AND DISCUSSION

Characteristics of coconut fiber hydrochar@ OCN graphitic carbon nitride composite

Scanning electron microscope (analysis

Surface morphology analysis was carried out using a scanning electron microscope (SEM) to see the surface of coconut fiber HC, OCN, and 10% hydrochar@OCN composites, which can be observed in Figure 1.

The hydrochar surface in SEM (Figure 1a) tests exhibits an irregular surface morphology, characterized by a coarse, porous, and fibrous structure (Zhou et al., 2019). In contrast, SEM observations of OCN (Figure 1b) reveal an agglomerated morphology composed of irregularly shaped fine particles. This structure exhibits an aggregation of g-C_3N_4 sheets stacked on top of each other, forming a porous structure with interparticle gaps. This characteristic is typical of thermally calcined graphitic carbon nitride, where g-C_3N_4 sheets tend to stack due to van der Waals forces between layers. The rougher appearance of the OCN surface indicates the success of the oxygen doping process.

Pure g-C_3N_4 (CN) material has a shape like two-dimensional (2D) layered sheets that are stacked on top of each other, with varying sizes (Putri et al., 2020). After the oxygen doping process, the sheet shape changes to a flake-like structure that shows the typical morphology of OCN. In general, the shape of OCN remains relatively unchanged, but the results indicate that OCN has smoother edges than pure g-C_3N_4. This is caused by the random oxidation reaction of oxalic acid during the synthesis process, which causes mild corrosion on the material surface.

The 10% hydrochar@OCN composite (Figure 1c) shows a greater HC dispersion on the composite surface, partially covering the OCN surface. The HC particles begin to aggregate, but still adhere

fairly well to the OCN structure. The HC layer thickens and partially covers the OCN pores. There is increased contact between OCN and HC, which can accelerate electron flow, but the aggregation that begins to form has the potential to slightly reduce the effective surface area. This composition is likely the optimal ratio, where the amount of OCN is sufficient to form many active sites without excessively covering the HC pores. As the density of HC particles on the surface increases, the HC layer begins to partially cover the OCN surface. Gaps/pores between particles are still visible, so surface access is relatively maintained. There are indications of more intense interactions between OCN and HC (extensive interphase contact).

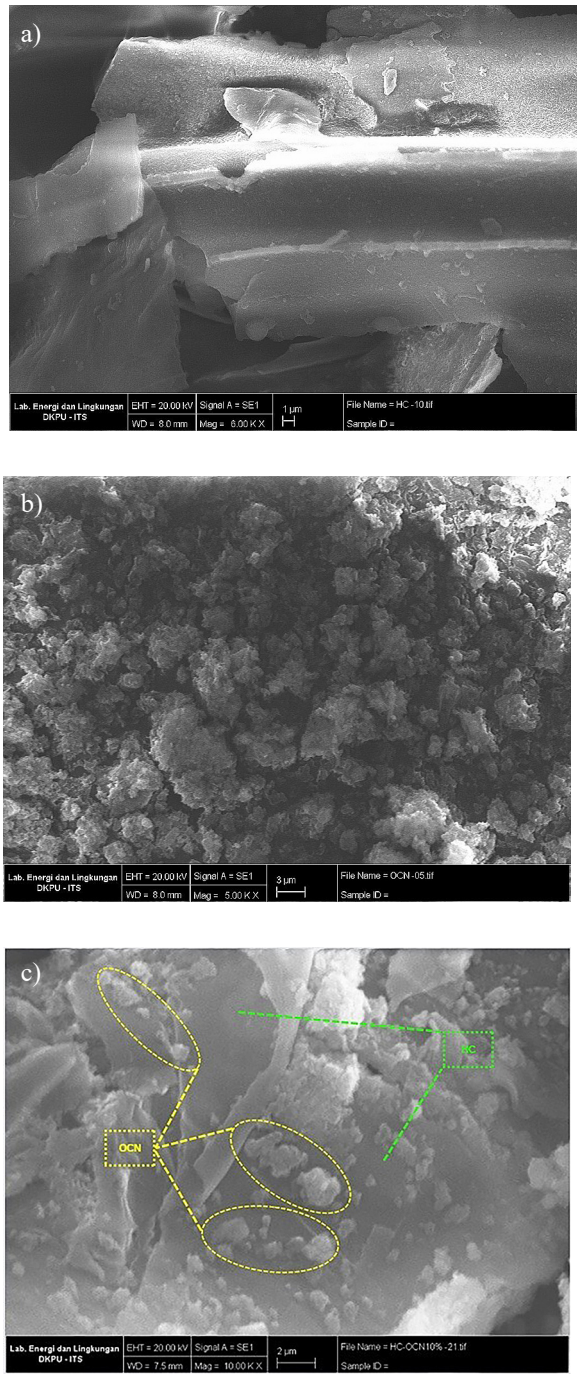

Figure 1. SEM results: (a) HC, (b) OCN, (c) hydrochar@OCN 10%

Energy dispersive X-ray (EDX) analysis

EDX analysis is used to identify and map the distribution of chemical elements on the surface of a solid material. This test is performed in conjunction with SEM and utilizes the characteristic X-rays emitted by elements in the sample when exposed to an electron beam. The results of the EDX test are shown in Figure 2 and Table 2.

Fourier transform infrared spectroscopy (FTIR) analysis

FTIR analysis is used to identify chemical functional groups at wave numbers (wavenumber, cm^{-1}) as seen in Figure 3. The FTIR spectra show that HC has many oxygen-containing functional groups. The peak at 1160 cm^{-1} indicates the presence of aliphatic C-O bonds, indicating that the HC surface is still rich in oxygen groups, while the peak at 1438 cm^{-1} indicates the presence of C-H bonds, indicating the presence of carboxylic groups. These groups are polar, so they can increase the attractive force between the HC surface and the surrounding polar molecules or ions (Prasannamedha et al., 2025). The peak at 1600 cm^{-1} indicates the presence of aromatic C=C bonds formed during hydrothermal carbonization (HTC). These aromatic groups can increase the structural stability of HC and strengthen the adsorption capacity through π-π stacking interactions with other aromatic organic molecules (Winingsih et al., 2016). The peak at 2923 cm^{-1} originates from the C=O stretching of the carboxyl group, and the peak at 3420 cm^{-1} indicates the presence of O–H groups from adsorbed water molecules. These results indicate that HC has many hydroxyl and carboxyl groups that can assist the photocatalytic process (Zhou et al., 2019). The presence of these groups is important because they can provide active sites for the formation of hydrogen bonds with target molecules (Zulfajri et al., 2024).

OCN material shows an absorption peak at 3,160 cm^{-1} associated with N-H stretching, indicating the presence of amine groups on the material surface that can increase hydrophilic properties and surface reactivity (Raturandang et al.,

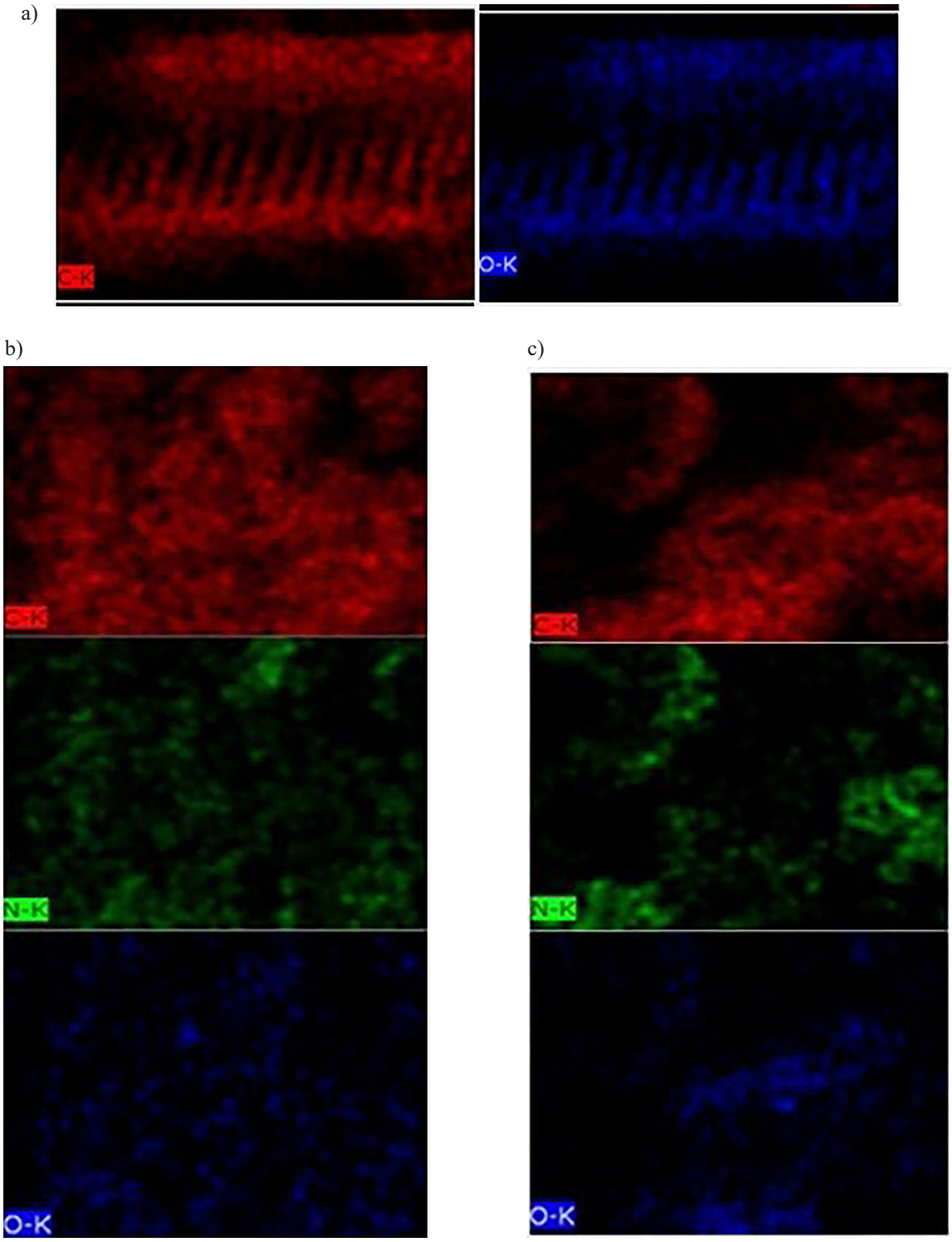

Figure 2. EDX results: (a) HC, (b) OCN, (c) hydrochar@OCN 10%

2022). The strong peak at 1.625 cm^{-1} is related to C=N stretching, which confirms the presence of aromatic nitrogen structures, especially heptazine and triazine rings, which are the main framework of g-C_3N_4 (Xie et al., 2018). In the range of 1394 cm^{-1} to 1083 cm^{-1}, significant peaks were detected originating from aromatic and heterocyclic C-N stretching, showing solid connectivity between aromatic rings (Shi et al., 2017).

The FTIR spectra of hydrochar@OCN 10% are similar to OCN, lacking distinct bonding peaks, likely due to the low oxygen content. This result confirms that O doping does not significantly affect the chemical structure of g-C_3N_4 (Liu et al., 2021). Furthermore,

Table 2. Percent of composition: HC, OCN, and hydrochar@OCN 10%

Material	N	C	O	Total
HC	0.00	54.42	45.58	100.00
OCN	44.56	42.05	13.39	100.00
HC/OCN 10%	42.17	35.25	22.58	100.00

Note: Laboratory test results, 2025.

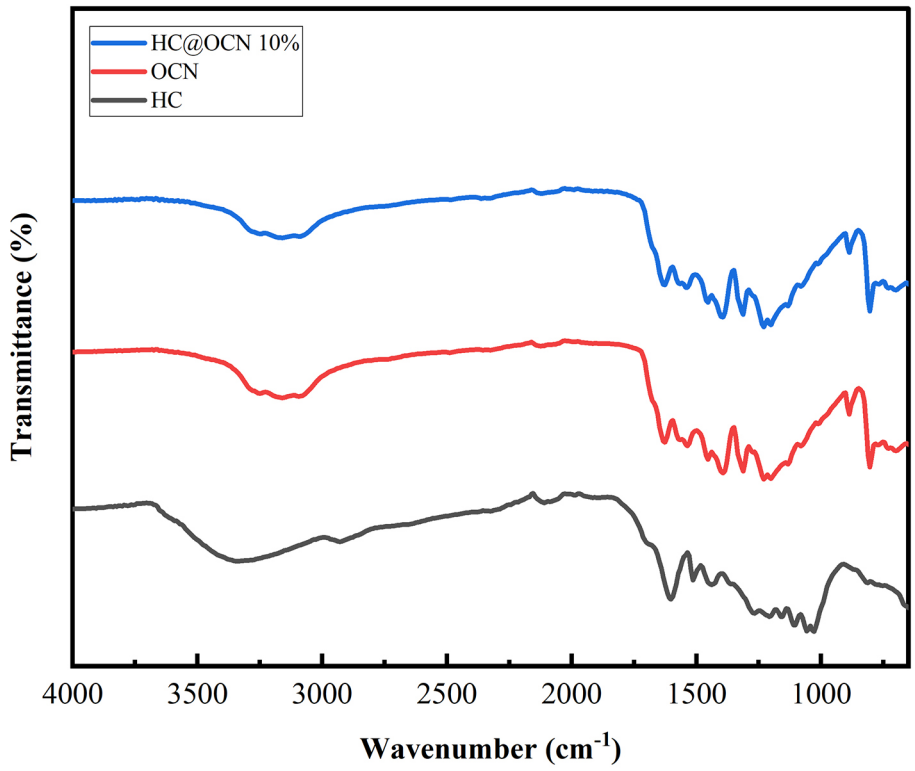

Figure 3. FTIR results: a) HC, b) OCN, c) hydrochar@OCN 10%

after the addition of HC, the characteristic peaks do not change drastically, indicating that HC does not alter the surface groups of OCN (Xu et al., 2022).

X-ray diffraction (XRD) analysis

XRD analysis allows the identification of crystal structures and the investigation of structural changes due to certain treatments, such as doping and composite formation. The following XRD results of HC, OCN, and hydrochar@OCN 10% are shown in the following Figure 4. The HC curve exhibits a broad signal, indicating the characteristics of hydrothermally treated carbon materials that are less crystalline/amorphous. The HC spectrum shows a broad peak centered at a 2θ value of 22.7°, representing the typical (200) crystal plane cellulose structure of amorphous carbon from HC (Li et al., 2021). The OCN sample exhibits two main peaks at 2θ angles of 12.8° and 27.6°. The peak at 12.8° corresponds to the (100) in-plane structure, while the peak at 27.6° corresponds to the (002) interlayer stacking of the g-C_3N_4 structure. These two peaks are characteristic of g-C_3N_4, originating from the repeating arrangement of interconnected tri-s-triazine and aromatic units (Wang et al., 2021). Compared with pure g-C_3N_4, the (002) peak in OCN shifts slightly from 27.4° to 27.6° because the addition of oxygen atoms has a higher electronegativity than nitrogen, so that when O replaces some of the N atoms, the interlayer bond becomes stronger. The distance is reduced (Liang et al., 2021). This peak shift also indicates a disruption in the crystal structure of g-C_3N_4 due to oxygen doping. In other words, some crystalline areas of g-C_3N_4 become more disordered after the addition of oxygen (Wang et al., 2008).

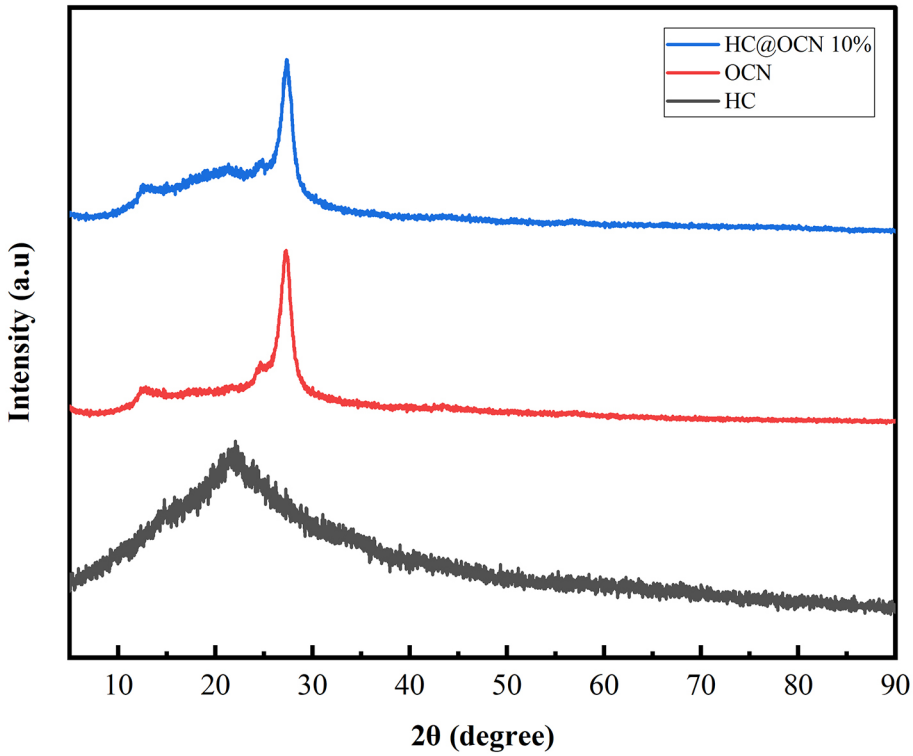

Figure 4. XRD results of HC, OCN, and hydrochar@OCN 10%

The hydrochar@OCN 10% did not exhibit significant changes in the XRD pattern, indicating that the addition of HC did not alter the crystal structure of OCN. However, the HC@OCN peak slightly shifted from 27.6° to around 27.8° caused by the interaction between HC and OCN, which caused a slight lattice contraction. The increase in the intensity of the diffraction peaks of hydrochar@OCN indicates the interaction between HC and OCN (Yao et al., 2007). In addition, there was no typical peak of HC in the XRD pattern of the hydrochar@OCN composite. This is because HC has low crystallinity and a small amount during the synthesis process.

Ultra violet diffuse reflectance spectroscopy analysis

UV-diffuse reflectance spectroscopy (UV-DRS) is used to evaluate the light absorption capacity of materials, especially in photocatalytic applications. The reflectance data were converted into absorbance using the Kubelka–Munk function. The band gap energies were estimated using the Tauc method. Since graphitic carbon nitride and its doped derivatives are well known as indirect band gap semiconductors, plots of versus photon energy were employed. The incorporation of hydrochar and oxygen doping resulted in a noticeable red shift and band gap narrowing, indicating improved visible-light absorption capability, which is beneficial for photocatalytic activity. The following Figure 5 shows the absorbance curves of HC, OCN, and hydrochar@OCN 10% composites.

HC material shows very low absorbance intensity across the entire wavelength range, both in the ultraviolet (UV) and visible (400–800 nm) regions. This indicates that HC contains many π-conjugated/amorphous carbon domains and surface groups that absorb across the entire light range. This provides light absorption capabilities but is not a semiconductor with a defined band gap like g-C_3N_4. HC can function as an electron conductor (electron-sink) when combined with a semiconductor, but is not effective as an e^-/h^+ (electron-hole) generator. Thus, the main function of HC in the composite system is likely more as a structural support material or as an electron transfer medium than as an active light-absorbing material (Zha et al., 2016).

OCN material displays an absorbance curve below a wavelength of 496 nm with a band gap value of 2.48 eV. This indicates that OCN has a good ability to absorb visible light, which is a typical characteristic of semiconductor materials (Liu

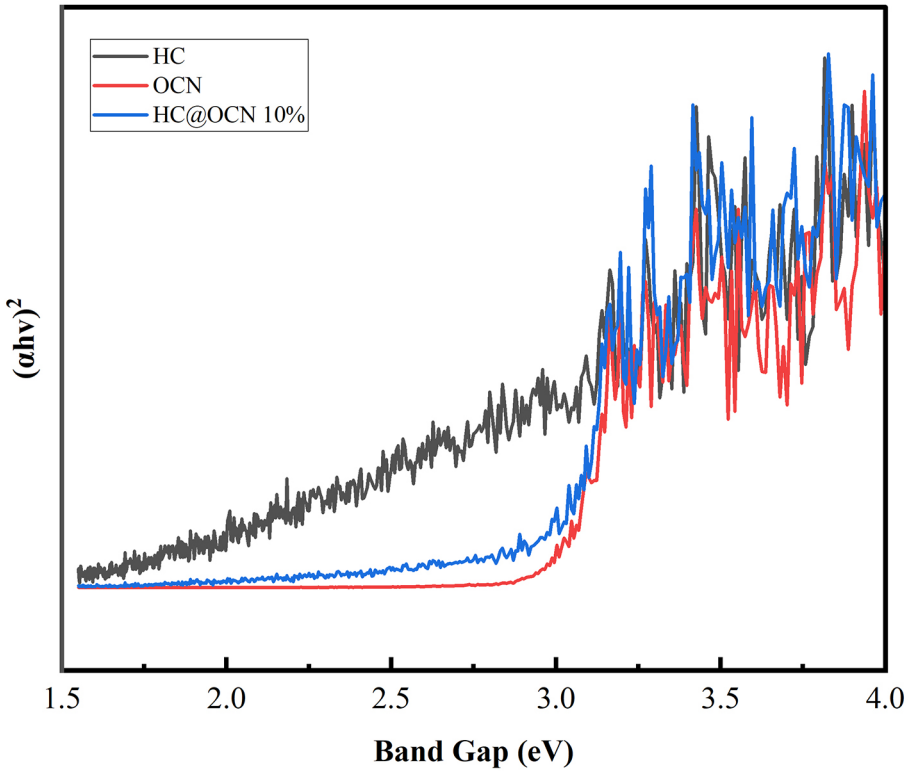

Figure 5. UV-DRS results of HC, OCN, and hydrochar@OCN 10%

et al., 2021). OCN maintains the semiconductor character of g-C_3N_4 with oxygen doping tending to provide defects/energy levels so that it can produce a red-shift (absorber slightly more visible) and increase charge separation (Bouzidi et al., 2020). Oxygen doping has a significant influence on its optical properties, where pure g-C_3N_4 (CN) without doping shows typical semiconductor behavior with limited absorption in the visible light region of 472 nm with a band gap value of 2.63 eV (Xu et al., 2019). This occurs due to the presence of oxygen atoms in g-C_3N_4. Modification of CN using oxalic acid has formed new energy levels, thereby reducing the band gap and increasing light absorption (Bouzidi et al., 2020).

In addition, the band gap of hydrochar@OCN 10% was calculated at 2.24 eV, respectively, indicating that the band gap decreased with increasing HC content (Xu et al., 2022). This indicates that the presence of HC begins to contribute to the increase in absorbance capacity (Pang et al., 2021). Hybridization with HC can reduce the band gap of the composite photocatalyst, thereby increasing light absorption (Zhou et al., 2019). The visible light absorption capacity of the hydrochar@OCN sample increased in the range of 500–560 nm, indicating that the addition of HC increases the visible light absorption capacity (Huang et al., 2020).

Brunauer-Emmett-Teller (BET) analysis

The nitrogen adsorption-desorption isotherms of HC, OCN, and hydrochar@OCN composites with different hydrochar loadings (1%, 10%, and 20%) are presented in Figure 6. All samples exhibit adsorption–desorption behavior characteristic of type IV isotherms (characteristic of mesoporous materials, which possess pore sizes in the range of 2–50 nm) with a pronounced hysteresis loop at high relative pressure ($P/P_0 > 0.4$), indicating the presence of mesoporous structures, which are favorable for adsorption and photocatalytic reactions involving relatively large organic molecules such as enrofloxacin.

Pristine hydrochar shows the lowest nitrogen uptake over the entire relative pressure range, reflecting its relatively limited accessible surface area and less-developed porosity. This behavior is typical of biomass-derived hydrochar, which generally consists of amorphous carbon domains with partially collapsed pore structures. In contrast, OCN exhibits a significantly higher adsorption capacity, particularly at high relative pressures. The sharp increase in nitrogen uptake near

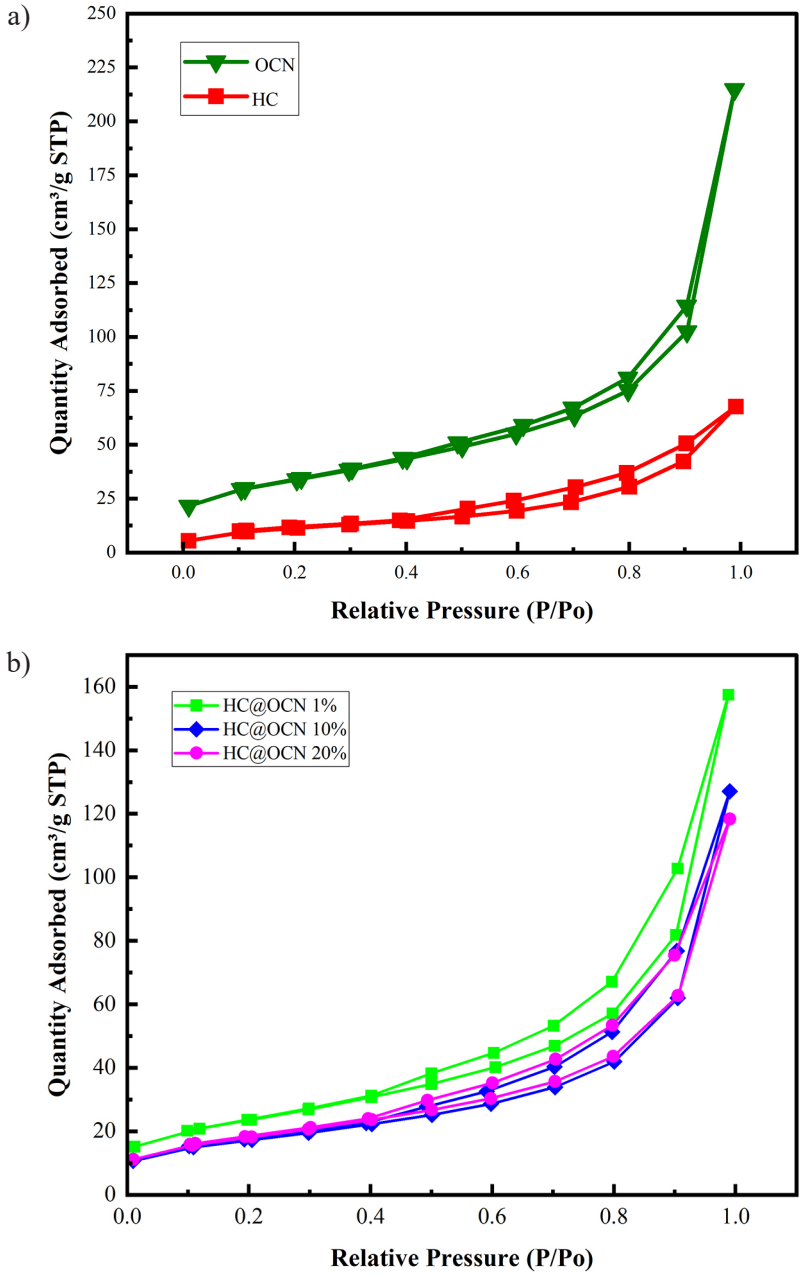

Figure 6. BET graph: a) OCN and HC, b) hydrochar@OCN 1%, 10%, and 20%

$P/P_0 \approx 0.9–1.0$ suggests the presence of interparticle voids and slit-like mesopores formed by the stacking of g-C_3N_4 nanosheets. Oxygen doping is known to disrupt the planar stacking of g-C_3N_4 layers, thereby increasing accessible surface area and pore volume.

The hydrochar@OCN composites show distinct adsorption behaviors depending on hydrochar loading, indicating that the textural properties are strongly influenced by the composite composition. The hydrochar@OCN 1% sample exhibits the highest nitrogen uptake among the composites, particularly in the medium-to-high relative pressure region. This suggests that a small amount of hydrochar effectively acts as a structural spacer, preventing excessive restacking of OCN layers and promoting the formation of additional mesopores. As a result, the composite displays enhanced surface accessibility and pore connectivity.

The hydrochar@OCN 10% composite shows a slightly reduced adsorption capacity compared to hydrochar@OCN 1%, but still significantly higher than pristine HC. The preservation of mesoporosity in this sample indicates an optimal balance between hydrochar dispersion and g-C_3N_4 framework integrity. This balanced structure provides sufficient surface area while maintaining effective

interfacial contact between HC and OCN, which is crucial for synergistic adsorption–photocatalysis processes.

The hydrochar@OCN 20% composite exhibits a further decrease in nitrogen adsorption capacity. Excessive hydrochar loading likely leads to partial pore blockage and agglomeration, which reduces the effective surface area and limits nitrogen diffusion into the pore network. This phenomenon explains the diminished textural properties observed at higher HC content.

The observed trend in BET results correlates well with the photocatalytic performance toward enrofloxacin degradation. Although hydrochar@OCN 1% exhibits the highest nitrogen uptake, hydrochar@OCN 10% demonstrates superior degradation efficiency due to the combined effects of sufficient surface area, improved adsorption capacity, and enhanced interfacial charge transfer between hydrochar and OCN.

Mechanism of how photocatalysts work

The photocatalytic mechanism is a crucial aspect in understanding the performance and effectiveness of a photocatalytic material in the degradation of organic compounds, including the antibiotic ENR. The photocatalytic mechanism is explained in Figure 7.

When the hydrochar@OCN composite is illuminated with visible light from a 460 nm blue LED, it absorbs photons whose energy matches its band gap. This photon absorption results in the excitation of electrons from the valence band to the conduction band, leaving holes (h^+) in the valence band (Uddin et al., 2025; Lan et al., 2024). After the formation of electron-hole pairs (e^-/h^+), charge transfer occurs between the materials through the heterojunction contact between the HC and OCN. The potential energy difference between the two materials causes the excited electrons to move toward the lower-energy conduction band (CB), while the holes (h^+) move to the higher-energy valence band (VB) (Wu et al., 2018). The role of HC here is crucial as an electron mediator, helping to accommodate electrons and facilitate their transfer to oxygen molecules temporarily adsorbed on the surface (Amelia et al., 2023). Electrons that have moved to the conduction band (CB) then interact with oxygen molecules (O_2) around the photocatalyst surface. When the conduction band (CB) position of the hydrochar@OCN composite is sufficiently negative with respect to the O_2/O_2^- reduction potential, the electrons can reduce oxygen to superoxide radicals (O_2^-). This species is the primary oxidant in the system, which can react directly with organic molecules or form singlet oxygen ($^1O_2$) through energy transfer. Both species are highly reactive and can attack various positions in the ENR structure.

In contrast, the formation of hydroxyl radicals (OH^-) from the oxidation of water by holes in the valence band is not significant. This is because the valence band (VB) energy position of

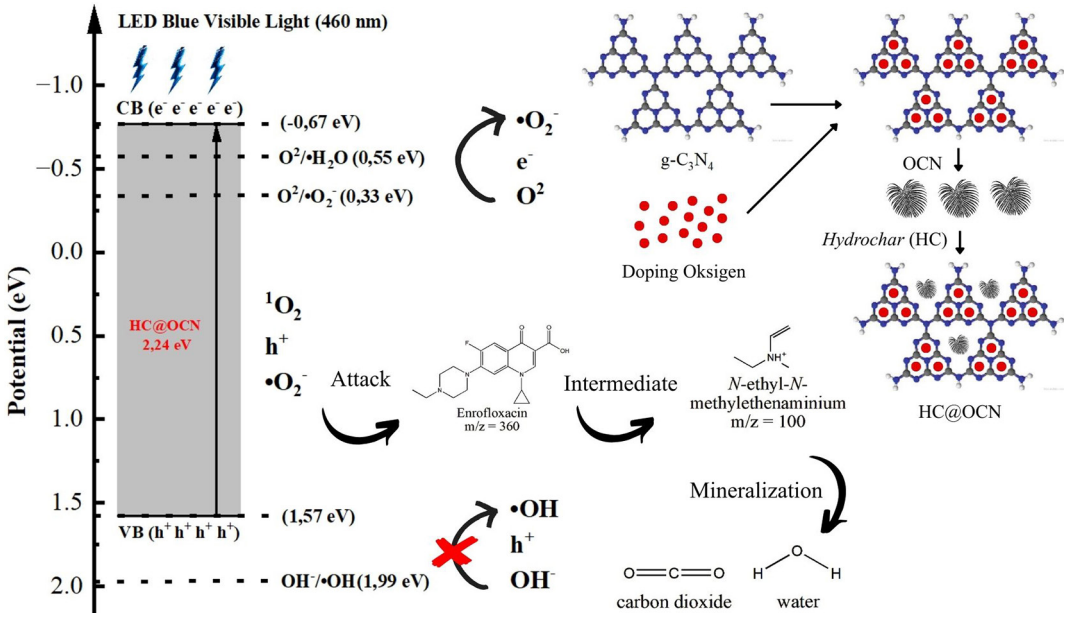

Figure 7. Photocatalytic process mechanism

the hydrochar@OCN composite is not positive enough to oxidize H_2O to •OH. The remaining holes (h^+) in the valence band (VB) not only play a passive role but can also directly oxidize ENR molecules that have been adsorbed on the composite surface.

Performance of the photocatalysis process using hydrochar@OCN composite

Effect of composite composition

The composition of the Hydrochar@OCN composite also had a strong impact on the photocatalytic efficiency. Variations included pure OCN, pure hydrochar, and composites containing 1%, 10%, and 20% hydrochar relative to the OCN mass. The optimum degradation efficiency of 70.29% was obtained with the hydrochar@OCN 10% composite after 60 minutes. This is because the amount of 10% HC is not too much and not too little compared to 1% and 20% HC, thus optimizing the adsorption process without disrupting the performance of OCN. This improvement can be explained by the synergistic interaction between the two components. Hydrochar provides abundant surface functional groups and a porous structure that enhances ENR adsorption, while OCN contributes to visible-light activation and ROS generation (Rasheed et al., 2019). The 10% loading ratio strikes the best balance between adsorption and photocatalytic activity. Removal results of ENR shows in Figure 8.

Lower hydrochar content 1% (60.50%) results in insufficient surface area to facilitate adsorption, while excessive hydrochar loading 20% (65.21%) may shield g-C_3N_4 from light or block its active sites, reducing photoactivation efficiency. Therefore, the hydrochar@OCN 10% composite provides the most favorable structure-function relationship, optimizing charge transfer, surface reactivity, and light absorption. The synergistic interaction between the adsorptive and photoactive components can explain this improvement. Hydrochar (55.79%) offers a porous structure, a high surface area, and abundant oxygen-containing functional groups ($COOH^-$, OH^-) that facilitate ENR adsorption and enhance pollutant–catalyst contact. Meanwhile, O-doped g-C_3N_4 (50.72%) acts as the visible-light-responsive semiconductor responsible for generating charge carriers (e^-/h^+ pairs) (Xiao et al., 2021). The integration of HC into OCN improves charge separation and electron mobility, as HC serves as an electron mediator,

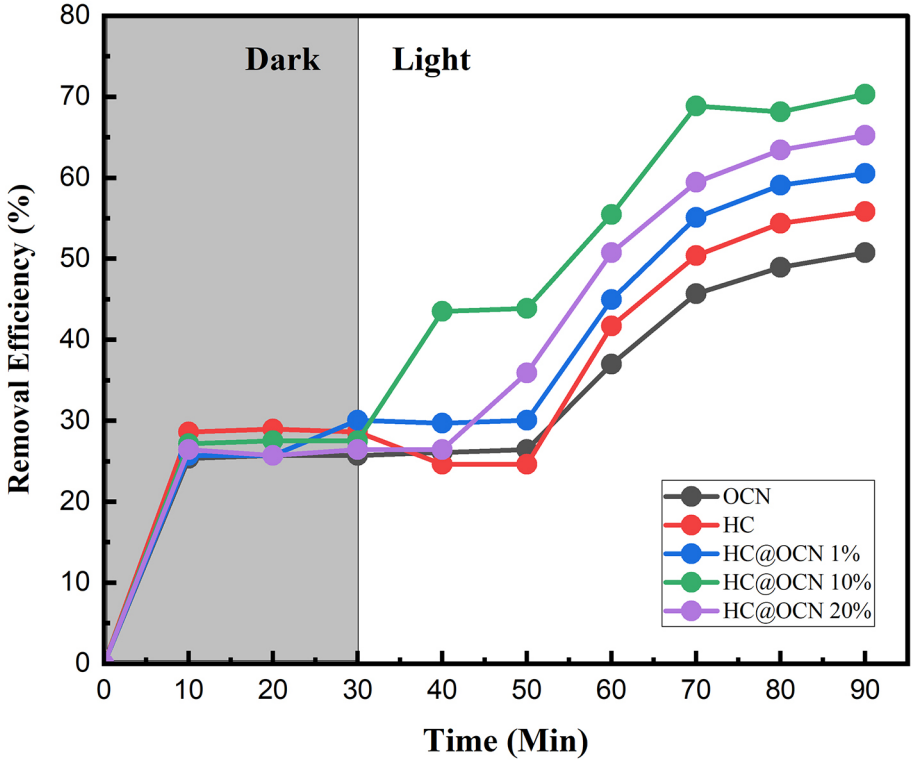

Figure 8. Effect of composite composition

minimizing recombination losses and enhancing ROS generation (Guo et al., 2021).

However, excessive hydrochar content (20%) may block active photocatalytic sites or cause light shielding, which reduces photon absorption by OCN. Additionally, agglomeration of excess carbon material can reduce catalyst dispersion and electron transport efficiency (Meng et al., 2020). Conversely, composites with very low HC content (1%) fail to provide sufficient adsorptive sites to enhance surface reactions. Therefore, a 10% HC ratio provides the optimal balance between adsorption enhancement and photocatalytic activation, leading to superior degradation performance.

Effect of catalyst dosage

Catalyst dosage plays a crucial role in determining the number of available active sites and the extent of light utilization. The degradation efficiency increased with increasing catalyst dosage from 1 g/L to 3 g/L (Figure 9). The highest removal efficiency of 94.20% was achieved at 3 g/L, 1 g/L (72.10%), 1.5 g/L (76.08%), 2 g/L (82.97%), and 2.5 g/L (88.76%) indicating that a larger amount of catalyst provides more active surface area for adsorption and enhances photon absorption, which promotes greater ROS generation (Abubakar and Nuraddeen, 2020).

At lower dosages (1–1.5 g/L), the number of available active sites is limited, which restricts both ENR adsorption and photon absorption, leading to lower degradation efficiency. As the catalyst dosage increases, more active sites become available for ENR molecules to adsorb, and the generation of photoexcited charge carriers increases proportionally (S. Wu et al., 2021). This enhances the production of hydroxyl and superoxide radicals, thereby accelerating degradation kinetics. However, photocatalysis does not always improve linearly with catalyst loading (Rodríguez-Chueca et al., 2023). Beyond the optimal dosage, particle aggregation and light scattering can occur, reducing the penetration of light through the suspension. This leads to a shielding effect, where some catalyst particles block others from receiving light. Therefore, 3 g/L represents the equilibrium point where the number of active sites and light absorption efficiency are both maximized without inducing light attenuation (Horn and Gremetz, 2020).

Therefore, at lower dosages (1–1.5 g/L), degradation was limited by insufficient active sites and fewer ROS, leading to slower reaction rates. Although further increasing the catalyst concentration could theoretically continue enhancing the reaction, excessively high dosages might lead to

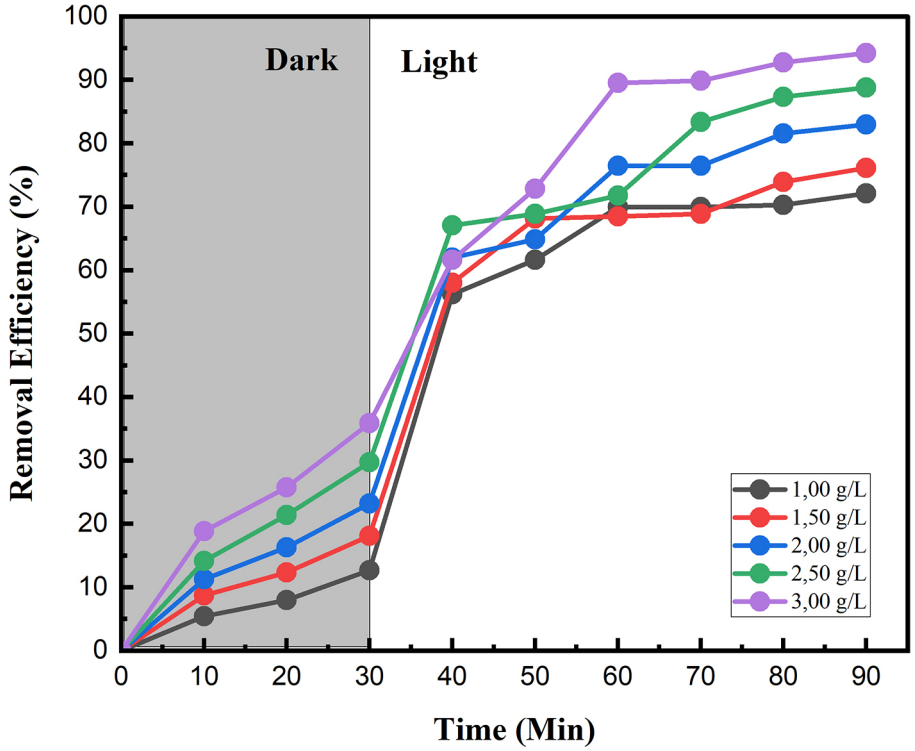

Figure 9. Effect of catalyst dosage

turbidity and light scattering, which reduces light penetration (Xiong et al., 2024). In this study, 3 g/L represented the optimal balance between active site availability and light absorption.

Effect of initial enrofloxacin concentration

The degradation performance was inversely related to the initial ENR concentration (Figure 10). The highest removal efficiency (94.93%) was obtained at 3 mg/L, while efficiency gradually decreased at higher concentrations (down to 88% at 10 mg/L). at 5 mg/L (93.47%), 7 mg/L (91.30%), 9 mg/L (88.94%), 10 mg/L (88.11%). This phenomenon is explained by the competition among ENR molecules for a limited number of active sites and ROS. At low concentrations, sufficient ROS and catalyst surface area are available to completely degrade ENR molecules. However, as the concentration increases, the ratio of ROS to pollutant molecules decreases, leading to partial degradation and slower kinetics (Yu et al., 2023). Moreover, higher ENR levels increase solution opacity, hindering light penetration and consequently reducing ROS formation. Therefore, lower initial concentrations favor faster reaction kinetics and higher degradation efficiency. High pollutant loading can increase the formation of intermediate degradation products that occupy catalyst surfaces, inhibiting further oxidation. This observation is consistent with the Langmuir–Hinshelwood kinetic model, which describes how, at higher substrate concentrations, surface saturation limits the reaction rate (Tran et al., 2023). Thus, maintaining moderate ENR levels (around 3–5 mg/L) ensures sufficient ROS availability and minimizes diffusion and light attenuation constraints. An HPLC test is carried out to confirm the results of the UV-vis test because it has higher accuracy.

pH effect of enrofloxacin

Solution pH substantially affects photocatalytic degradation (Figure 11) by altering the surface charge of the catalyst and the ionization state of ENR. The maximum efficiency (70.29%) was achieved at pH 7, 50.36% at pH 2, 60.14% at pH 4, 40.21% at pH 10, and 30.79% at pH 12, indicating that neutral conditions are optimal for both adsorption and ROS generation.

At pH 7, ENR exists mainly in a zwitterionic form, minimizing electrostatic repulsion between the pollutant and the catalyst surface. This facilitates stronger adsorption and efficient radical attack. Under acidic conditions (pH 2–4), the catalyst surface becomes positively charged, leading to electrostatic repulsion with protonated ENR molecules, while excess H^+ ions can scavenge

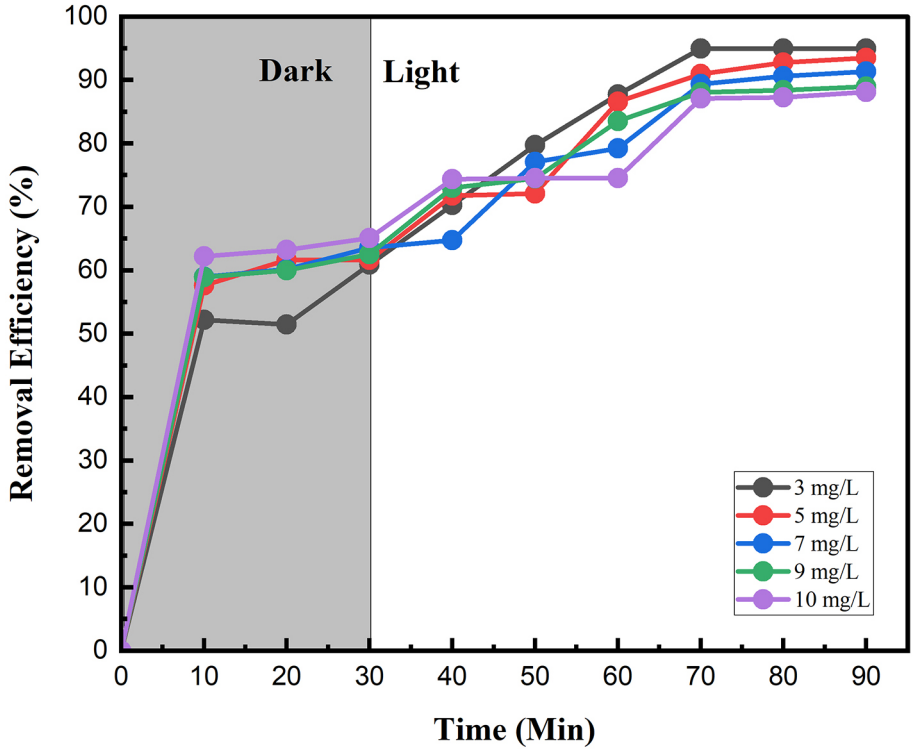

Figure 10. Effect of initial ENR concentration

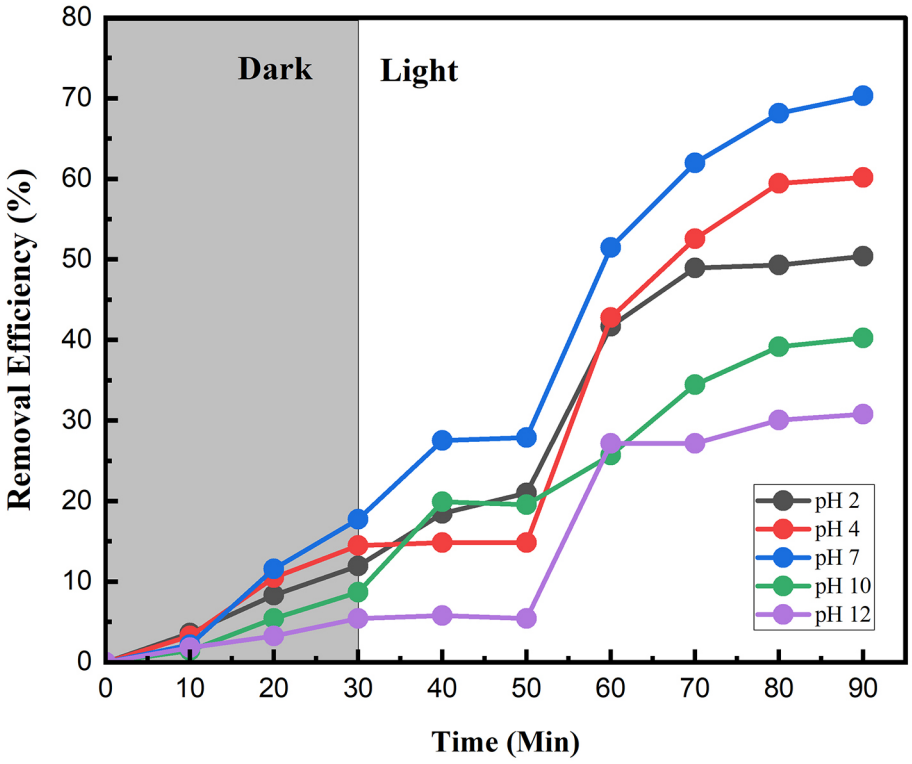

Figure 11. pH effect of ENR

photogenerated electrons, decreasing ROS formation. At basic conditions (pH 10–12), the negatively charged catalyst surface repels deprotonated ENR species and may lead to OH^- competition for oxidation sites, reducing degradation efficiency (Zhang et al., 2024). Thus, maintaining a neutral pH ensures optimal interaction between the catalyst and pollutant and promotes balanced ROS generation for efficient ENR photodegradation.

At acidic conditions (pH 2–4), the catalyst surface becomes positively charged, resulting in electrostatic repulsion with the protonated ENR species. Furthermore, excess H^+ ions act as electron scavengers, capturing photogenerated electrons and reducing ROS production. Conversely, in basic conditions (pH 10–12), the surface becomes negatively charged, causing repulsion with deprotonated ENR anions (Guo et al., 2024). Excess OH^- ions can also compete with ENR for active sites and scavenge photogenerated holes, thus diminishing oxidative efficiency. Therefore, the neutral environment (pH 7) provides the best alignment between pollutant ionization, catalyst surface charge, and ROS generation dynamics, leading to optimal photocatalytic degradation performance (Bendjama and Hamdaoui, 2025).

The pHPZC of hydrochar@OCN was not experimentally determined in this study. Nevertheless, pH-dependent degradation trends were discussed based on known surface charge behavior of carbon nitride and hydrochar. Future studies will include pHPZC determination to strengthen electrostatic interaction analysis.

Effect of water matrix

The type of water matrix significantly influenced the photocatalytic degradation of enrofloxacin (ENR) using the hydrochar@O-doped g-C_3N_4 composite (Figure 12). It should be noted that detailed physicochemical parameters of the water matrices, such as pH, conductivity, total dissolved solids, and dominant ion concentrations, were not measured in this study. Therefore, a quantitative correlation between specific inorganic ions and photocatalytic degradation efficiency could not be established. Nevertheless, the observed changes in enrofloxacin removal efficiency qualitatively reflect the influence of complex water matrices, which is consistent with previous reports where inorganic ions and natural organic matter act as radical scavengers or compete for active sites on the catalyst surface. Among the tested matrices, lake, river, rain, spring, and deionized (DI) water, the highest degradation efficiency after 60 minutes was achieved in DI water (70.29%). This superior performance is attributed to the purity of DI water,

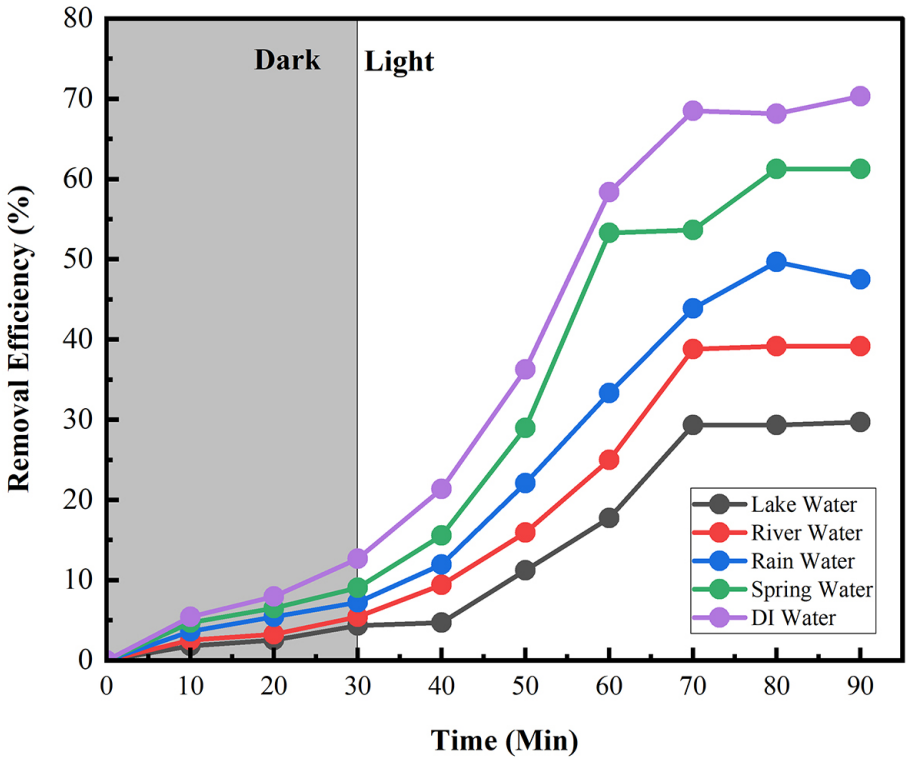

Figure 12. Effect of water matrix

which contains no interfering ions, turbidity, or natural organic matter (NOM) (Lin et al., 2023). These conditions allow maximum light penetration and unimpeded generation of reactive oxygen species (ROS) such as OH^- and O_2^- radicals, both essential for oxidative degradation.

In contrast, the degradation efficiencies in natural waters such as lake (47.48%), river (53.26%), rainwater (61.23%), and spring water (61.23%) were noticeably lower. This decline can be explained by the scavenging effect of inorganic ions (e.g., Cl^-, HCO_3^-, SO_4^{2-}, and NO_3^-), which react competitively with ROS, reducing their availability for pollutant oxidation. Chloride ions, for instance, can react with hydroxyl radicals to form less reactive species (Cl^- or Cl_2^-), thereby diminishing oxidative capacity (Velo-Gala et al., 2023). Similarly, bicarbonate ions act as hydroxyl radical scavengers by forming carbonate radicals (CO_3^-), which exhibit significantly lower redox potential.

Furthermore, natural organic matter (humic and fulvic acids) present in surface waters can absorb visible light, limiting photon availability for the photocatalyst, and also compete with ENR for adsorption sites (Gowland et al., 2021). The combined effects of light attenuation, ion interference, and radical quenching explain the lower performance observed in non-DI matrices. These findings are consistent with reports that photocatalytic processes exhibit maximum activity in low-ionic-strength media due to enhanced ROS lifetime and surface charge stability. Conversely, natural waters such as lakes, rivers, and rainwater exhibited lower degradation efficiencies (ranging from 47% to 61%), primarily due to the presence of inorganic ions (e.g., Cl^-, SO_4^{2-}, HCO^{3-}) and dissolved organic carbon that compete with ENR for ROS and may quench photogenerated radicals (Fattahi et al., 2021). The result demonstrates that ionic strength and organic impurities are critical inhibitors in photocatalytic processes, confirming that DI water represents the ideal medium for maximizing catalyst performance.

Kinetic analysis

The adsorption kinetics of enrofloxacin onto the hydrochar@OCN composite were analyzed using several kinetic models, including pseudo-first-order, pseudo-second-order, and intraparticle diffusion models. Among these, the pseudo-second-order model exhibited the best fit, as evidenced by the highest correlation coefficient (R^2 = 0.9897) and good agreement between the calculated and experimental adsorption capacities (Figure 13).

Based on the pseudo-second-order model, the equilibrium adsorption capacity (q_e) and the rate constant (k_2) were determined to be 7.93 mg g^{-1} and 0.086 g mg^{-1} min^{-1}, respectively. The relatively high k_2 value suggests a rapid adsorption process, which is beneficial for practical applications.

The excellent fitting of the pseudo-second-order model implies that the adsorption process is mainly governed by chemisorption, involving strong interactions between enrofloxacin molecules and the active functional groups on the hydrochar@OCN surface. These interactions may include hydrogen bonding, π–π interactions, and electrostatic attraction mediated by oxygen-containing functional groups on hydrochar@OCN.

Statistic test (multiple regression)

A multivariable experimental design was employed to evaluate the effects of key operational factors on the degradation performance of enrofloxacin. Four independent variables were selected as fixed factors: composite dosage (X1), composite composition (X2), initial enrofloxacin concentration (X3), and solution pH (X4). Each factor was investigated at five predefined levels to systematically assess its individual and combined influences on the photocatalytic degradation efficiency. The fixed-factor approach was chosen to ensure controlled and reproducible experimental conditions while enabling the evaluation of parameter sensitivity. This factorial design allowed for a comprehensive analysis of the relative importance of each variable and facilitated the identification of optimal operational conditions for enrofloxacin degradation using the hydrochar@OCN composite (Figure 14 and 15).

The analysis of variance (ANOVA) results indicate that all investigated factors, composite dosage (X1), composite composition (X2), enrofloxacin concentration (X3), and pH (X4), significantly affected the removal efficiency of enrofloxacin. This is evidenced by the high F-values and p-values below 0.001 for all factors. Among them, pH (X4) exhibited the largest adjusted sum of squares (Adj SS = 6781.8) and the highest F-value (103.22), indicating that pH was the most dominant factor influencing the photocatalytic degradation performance. The strong influence of pH is associated with its role in controlling surface charge properties of the photocatalyst, ionization state of enrofloxacin, and the generation and stability of reactive oxygen species. Composite composition (X2) and enrofloxacin concentration (X3) also showed substantial contributions, with Adj SS values of 2110.7 and 1788.4, respectively, suggesting that material formulation and pollutant loading significantly affect degradation efficiency. Meanwhile, composite dosage (X1) contributed the least among the studied factors (Adj SS = 1181.9), although it remained statistically significant, indicating that increasing catalyst dosage enhances removal efficiency to a certain extent. Overall, the relatively low error mean square (16.43) demonstrates good experimental precision and confirms that the selected factors adequately explain the observed variability in enrofloxacin removal efficiency

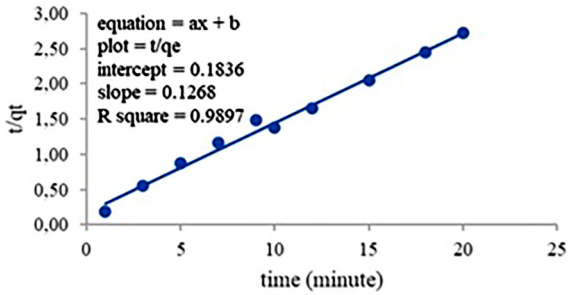

Figure 13. Pseudo-second order

Factor Information

Factor	Type	Levels	Values
Dosis Komposit (X1)	Fixed	5	A1, A2, A3, A4, A5
Komposisi Komposit (X2)	Fixed	5	B1, B2, B3, B4, B5
Konsentrasi ENR (X3)	Fixed	5	C1, C2, C3, C4, C5
pH (X4)	Fixed	5	D1, D2, D3, D4, D5

Figure 14. ANOVA test data

Analysis of Variance

Source	DF	Adj SS	Adj MS	F-Value	P-Value
Dosis Komposit (X1)	4	1181.9	295.47	17.99	0.000
Komposisi Komposit (X2)	4	2110.7	527.67	32.13	0.000
Konsentrasi ENR (X3)	4	1788.4	447.09	27.22	0.000
pH (X4)	4	6781.8	1695.46	103.22	0.000
Error	43	706.3	16.43		
Total	59	21101.3			

Figure 15. ANOVA test result

Enrofloxacin degradation pathway using hydrochar@OCN composite

The photocatalytic mechanism is an important aspect in understanding the performance and effectiveness of a photocatalyst material in the

degradation process of organic compounds, including the antibiotic enrofloxacin. Hydrochar@OCN composites are designed to optimize photocatalytic activity under visible light by combining the light-absorbing properties of OCN with the adsorptive ability and electron conductivity of hydrochar.

Liquid chromatograph-mass spectrometry analysis

A liquid chromatography-mass spectrometry (LC-MS) test was conducted to identify the degradation compounds and determine the changes in the molecular structure of enrofloxacin after the photocatalytic process using the coconut fiber hydrochar@O-doped g-C_3N_4 composite. This analysis combines the ability of liquid chromatography to separate compound components with highly sensitive mass detection from a mass spectrometer. Through the results of the chromatogram and mass spectrum obtained, differences in retention time values and mass to charge ratio (m/z) between the initial compound ENR and the degradation products can be identified. This difference indicates the occurrence of a photodegradation process that produces derivative compounds with lower molecular mass, indicating the breaking of chemical bonds due to the photocatalytic activity of hydrochar@OCN under visible light irradiation. The results of the LC-MS test are presented in Figure 16.

Based on the results of the LC-MS test, the chromatogram in Figure 11a displays the spectrum of a standard enrofloxacin sample, featuring a major peak at m/z 360 and a minor peak at around m/z 382. The dominant peak indicates the presence of the main ENR molecule that has not undergone degradation. In contrast, the minor peak can be interpreted as an ionization fragment of the ENR structure that corresponds to the typical $[M^+H]^+$ ion of enrofloxacin. The enrofloxacin degradation pathway generally involves three main mechanisms, namely: (i) substitution

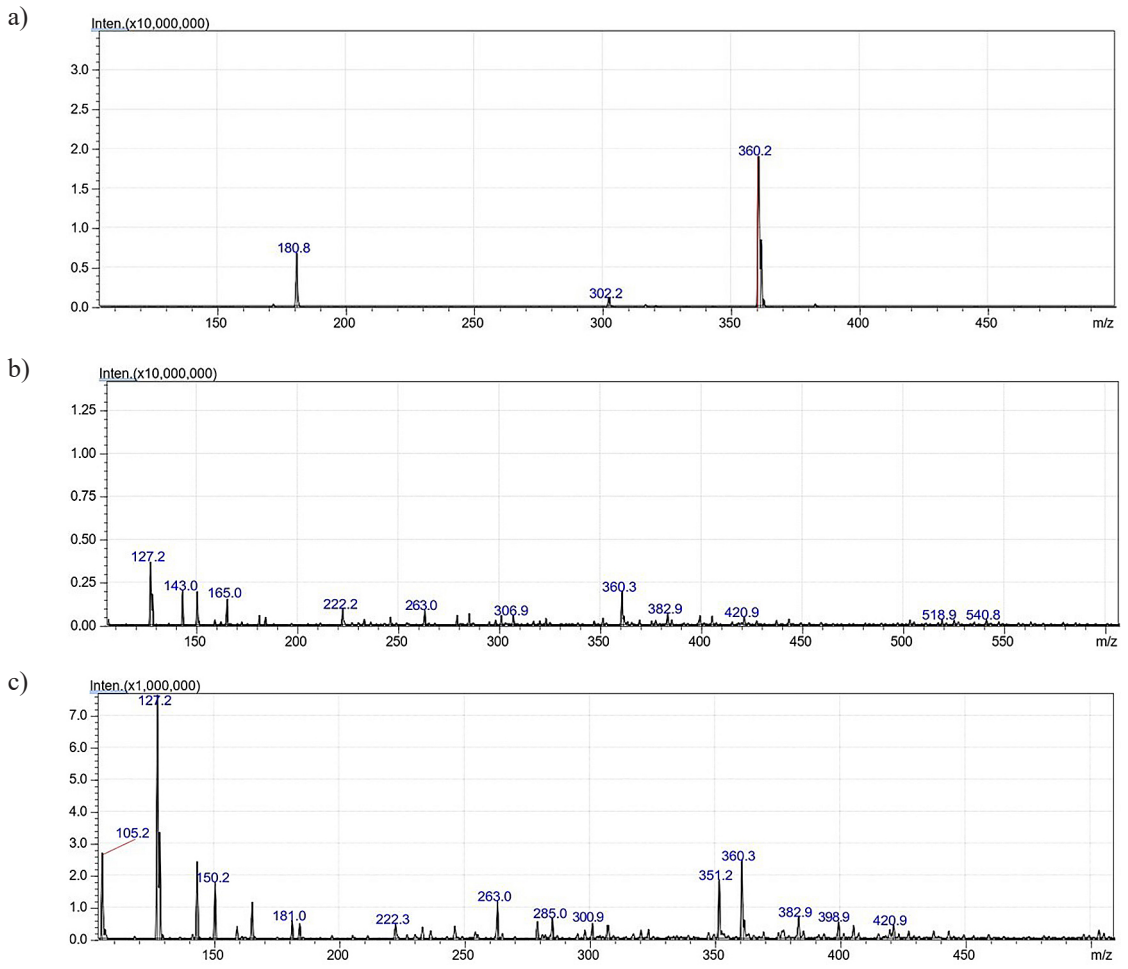

Figure 16. LCMS results analysis: (a) ENR before photodegradation, (b) ENR photodegradation at 30 minutes (sample A), (c) ENR photodegradation at 60 minutes

or loss of the piperazine group, (ii) cleavage and decarboxylation of the quinolone ring, and (iii) substitution or loss of fluorine atoms (Xu et al., 2025a). The identified degradation products can be grouped into several transformation pathways. The first pathway involves an N-dealkylation reaction on the piperazine ring (Melent'ev & Kataev, 2015).

LC-MS analysis of sample A (Figure 16b) showed that enrofloxacin (ENR) experienced degradation, which was indicated by the appearance of several new chromatogram peaks at different retention times compared to the parent compound. In the total ion chromatogram (TIC), the dominant peak of enrofloxacin was detected at a retention time of 5.873 minutes with m/z 360 and an area proportion of 82.75%, which is the typical molecular mass of ENR. LC-MS Analysis of Sample B (Figure 16c), the peak at m/z 360 still appeared but with a significantly decreased in: the peak at m/z 360 still appeared but with significantly reducedtensity, clearly detected at RT 5.89 minutes with an area proportion of 74.78%, indicating that most of the ENR molecules had undergone degradation. In addition, several new peaks appeared, indicating the enrofloxacin degradation pathway at m/z 105, 127, 150, and 263, which were not found in the standard ENR sample, indicating the formation of derivative compounds resulting from the cleavage of chemical bonds from the enrofloxacin structure, such as cleavage of the piperazine ring or loss of the carboxylate group.

Degradation pathway of enrofloxacin

The results of LC-MS analysis showed that the degradation process of enrofloxacin (m/z 360) produced several intermediate compounds with the main m/z values of 390, 302, 279, 274, 249, 164, 157, 151, 114, and 110. Based on the differences in mass and structure of the fragments formed, the degradation mechanism of enrofloxacin can be explained through four main pathways (degradation pathways) as shown in the following Figure 17.

Pathway 1 (Quinolone ring cleavage)

Active radicals attack the C–N and C–C bonds in the quinolone structure, producing products with m/z 279 (3,6-dihydroxy-7-(hydroxy(2-nitrosoethyl) amino)-1-methylquinolin-4(1H)-one) and m/z 151 (1-(2-aminophenyl) ethanone)) which then undergoes defluorination and decarboxylation to form a compound with m/z 151. This process decreases aromatic stability and accelerates fragmentation into oxidized benzoic acid derivatives. This stage is important because it marks the beginning of the degradation of the fluoroquinolone core framework (Sun et al., 2024).

Pathway 2 (Advanced fragmentation and mineralization)

Compounds with a low m/z (274) were identified as advanced fragmentation products of aromatic structures undergoing oxidation and C–C bond cleavage. Some of these, such as 4-aminophenol (m/z 110) and N-ethyl-N-methyl-ethelaminium (m/z 100), are simpler compounds and are easily further oxidized to CO_2 and H_2O (Pei et al., 2023). This indicates that the degradation process has reached the partial mineralization stage, indicating the success of the photocatalytic system in decomposing the complex structure of enrofloxacin.

Pathway 3 (F group substitution and decarboxylation)

The tightly bound fluorine at the C-6 position is substituted by a hydroxyl group due to the electrophilic attack of the •OH radical, producing m/z 302 (7-fluoro-2-hydroxy-4-methyl-6-(4-methylpiperazin-1-yl) naphthalen-1(4H)-one). This product then undergoes decarboxylation and dealkylation reactions on the piperazine side, forming compounds with m/z 338 and 250 (Wei et al., 2024). At m/z 164, deflorination and decarboxylation processes occur. The initial stage of enrofloxacin degradation involves the cleavage of the C–N bond in the piperazine ring and the loss of the carboxylic group (-COOH), producing a simpler quinolinol derivative, namely 6-fluoro-1,4-dihydroquinolin-4-ol. This process is usually caused by an oxidative reaction that occurs due to hydroxyl radicals (•OH) produced in the photocatalysis process (Xu et al., 2025b).

The cleavage of the quinoline ring and the formation of a simple aromatic compound occur at m/z 151. The compound 6-fluoro-1,4-dihydroquinolin-4-ol undergoes heterocyclic ring opening and removal of the fluoro group (F-). The result is 1-(2-aminophenyl) ethanone, which has a single benzene ring with amine and carbonyl groups. This indicates a process of reducing the complexity of the aromatic structure towards a

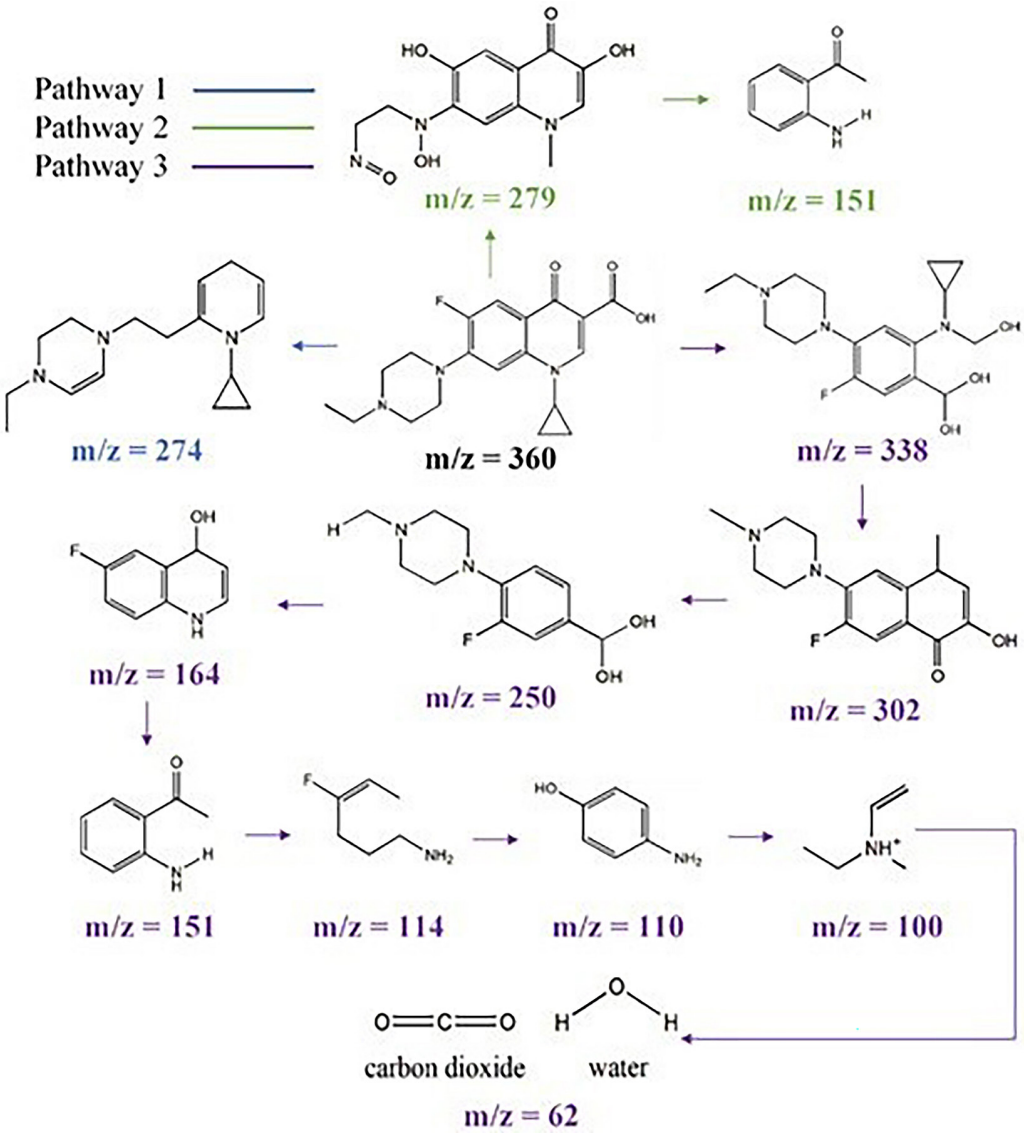

Figure 17. Degradation pathway of enrofloxacin

simpler molecule (Wang et al., 2025). At m/z 114, a partial deoxygenation and cyclization process occurs. From 1-(2-aminophenyl) ethanone, the C=O bond is broken, and cyclization produces a fluoroalkyl amine compound (m/z 114). This compound indicates further degradation of the aromatic nucleus towards an aliphatic structure, which is more easily oxidized further. This step also involves a partial reduction reaction at the carbonyl group and simplification of the carbon structure (Xu et al., 2025b).

Aromatization and hydroxylation processes occur at m/z 110, the fluoroalkyl amine compound then undergoes a hydroxylation reaction to produce 4-aminophenol. This compound is one of the common products of the degradation of phenolic derivatives of fluoroquinolone compounds. This process involves oxidation of the amine group and the formation of a hydroxyl group on the aromatic ring, which indicates increased hydrophilicity and facilitates further degradation (Xu et al., 2025b). At m/z 100, dimethylation, deamination, and carbon chain cleavage occur, which will then degrade to form CO_2 and H_2O. At this stage, the aromatic ring has completely decomposed, leaving a short-chain amine fragment (N-ethyl-N-methylethelaminium).

CONCLUSIONS

This study successfully demonstrated the potential of coconut husk-based hydrochar@OCN as an efficient photocatalyst for the degradation of

enrofloxacin under visible LED irradiation. Environmental and operational parameters, including the water matrix type, pH, catalyst dosage, composite composition, and initial ENR concentration, significantly influenced degradation efficiency. Among all tested conditions, deionized water provided the most favorable environment for photocatalysis due to the absence of interfering ions and organic matter. The composite containing 10% hydrochar in OCN achieved the highest photocatalytic activity, highlighting the synergistic effect between hydrochar's adsorption capacity and O-doped g-C_3N_4's photoactivity. Optimal degradation occurred at pH 7, where the balance between surface charge and pollutant ionization promoted efficient reactive oxygen species generation and pollutant adsorption. Under the optimal conditions of 3 g/L catalyst dosage and 3 mg/L initial ENR concentration, the composite achieved 94.20% and 94.93% removal efficiencies, respectively, within 60 minutes of illumination. These findings confirm that the hydrochar@OCN composite effectively enhances visible-light photocatalysis while utilizing sustainable biomass waste as a precursor. Overall, this work demonstrates a green and cost-effective approach for mitigating antibiotic pollution in water systems and provides valuable insights into how environmental factors govern photocatalytic efficiency. Future studies are recommended to explore catalyst reusability, scalability, and performance under natural sunlight for real wastewater applications.

Acknowledgements

The authors thank our colleagues from Institut Teknologi Sepuluh Nopember, who provided insight and expertise that greatly assisted the research. Thanks to the Ministry of Education, Culture, Research, and Technology (Kemendiktisaintek) for supporting this research with the Fundamental Research Fund No. 017/C3/DT.05.00/PL/2025.

REFERENCES

1. Abubakar A., Nuraddeen, A. (2020). Photocatalyst: A promising smart material in degradation of dye using response surface methodology Rsm. *Fudma Journal Of Sciences*, *4*(3), 591–600. https://doi.org/10.33003/fjs-2020-0403-328
2. Amelia, S. T. W., Nurtono, T., Setyawan, H., Widiyastuti, W. (2023). Electrocapacitive and electrocatalytic performances of hydrochar prepared by one-step hydrothermal carbonization without further activation. *Materials Research Express*, *10*(7), 1–17. https://doi.org/10.1088/2053-1591/ace75f
3. Bendjama, M., Hamdaoui, O. (2025). Photocatalytic degradation of safranin O: Unraveling the roles of dissolved gases, environmental matrices, and reactive species. *Catalysts*, *15*(9), 1–18. https://doi.org/10.3390/catal15090914
4. Bilal, M., Mehmood, S., Rasheed, T., Iqbal, H. M. N. (2020). Antibiotics traces in the aquatic environment: persistence and adverse environmental impact. *Current Opinion in Environmental Science & Health*, *13*, 68–74. https://doi.org/10.1016/j.coesh.2019.11.005
5. Bouzidi, A., Hussien, M. S. A., Abd-Rabboh, H. S. M., Abdelrhim, A. A. H., Yahia, I. S., Awwad, N. S. (2020). Physicochemical characterization of La-doped g-C3N4 for degradation of phenol and organic dye. *Desalination and Water Treatment*, *204*, 136–143. https://doi.org/10.5004/dwt.2020.26247
6. Chen, J., Fang, S., Shen, Q., Fan, J., Li, Q., Lv, K. (2022). Recent advances of doping and surface modifying carbon nitride with characterization techniques. *Catalysts*, *12*(9), 1–23. https://doi.org/10.3390/catal12090962
7. Fang, S., Zhang, W., Sun, K., Hu, Y. H. (2023). Highly efficient thermo-photocatalytic degradation of tetracycline catalyzed by tungsten disulfide under visible light. *Environmental Chemistry Letters*, *21*(3), 1287–1295. https://doi.org/10.1007/s10311-022-01526-6
8. Fattahi, A., Jaciw-Zurakowsky, I., Srikanthan, N., Bragg, L., Liang, R., Zhou, N., Servos, M., Arlos, M. (2021). Effect of Background Water Matrices on Pharmaceutical and Personal Care Product Removal by UV-LED/TiO2. *Catalysts*, *11*(5), 1–11. https://doi.org/10.3390/catal11050576
9. Gowland, D. C. A., Robertson, N., Chatzisymeon, E. (2021). Photocatalytic oxidation of natural organic matter in water. *Water*, *13*(3), 1–21. https://doi.org/10.3390/w13030288
10. Guo, H., Niu, C.-G., Liang, C., Niu, H.-Y., Yang, Y.-Y., Liu, H.-Y., Tang, N., Fang, H.-X. (2021). Highly crystalline porous carbon nitride with electron accumulation capacity: Promoting exciton dissociation and charge carrier generation for photocatalytic molecular oxygen activation. *Chemical Engineering Journal*, *409*, 1–12. https://doi.org/10.1016/j.cej.2020.128030
11. Guo, Y., Siretanu, I., Mugele, F., Mul, G., Mei, B. (2024). pH-Dependent photocatalytic performance of faceted BiOBr semiconductor particles in degradation of dyes. *Molecular Catalysis*, *553*, 1–8.

https://doi.org/10.1016/j.mcat.2023.113753

12. Horn, C. R., Gremetz, S. (2020). A method to determine the correct photocatalyst concentration for photooxidation reactions conducted in continuous flow reactors. *Beilstein Journal of Organic Chemistry*, *16*, 871–879. https://doi.org/10.3762/bjoc.16.78
13. Huang, X., Zhao, H., Zhang, G., Li, J., Yang, Y., Ji, P. (2020). Potential of removing Cd(II) and Pb(II) from contaminated water using a newly modified fly ash. *Chemosphere*, *242*, 1–10. https://doi.org/10.1016/j.chemosphere.2019.125148
14. Jiang, H., Li, X., Dai, Y. (2024). Phosphoric acid activation of cow dung biochar for adsorbing enrofloxacin in water: Icing on the cake. *Environmental Pollution*, *341*, 1. https://doi.org/10.1016/j.envpol.2023.122887
15. Lan, Y., Luo, Y., Yu, S., Ye, H., Zhang, Y., Xue, M., Sun, Q., Yin, Z., Li, X., Xie, C., Hong, Z., Gao, B. (2024). Cornstalk hydrochar produced by phosphoric acid-assisted hydrothermal carbonization for effective adsorption and photodegradation of norfloxacin. *Separation and Purification Technology*, *330*. https://doi.org/10.1016/j.seppur.2023.125543
16. Lin, X., Zhou, W., Li, S., Fang, H., Fu, S., Xu, J., Huang, J. (2023). Photodegradation of sulfamethoxazole and enrofloxacin under UV and simulated solar light irradiation. *Water*, *15*(3), 1–12. https://doi.org/10.3390/w15030517
17. Liu, A., Hu, J., He, J., Huang, X., Hu, N., Li, Y., Huang, Q., Guo, S., Liu, X., Yang, Z., Zhou, Y., Zou, Z. (2021). Direct Z-scheme hierarchical heterostructures of oxygen-doped g-C3N4/In2S3with efficient photocatalytic Cr(VI) reduction activity. *Catalysis Science & Technology*, *11*(24), 7963–7972. https://doi.org/10.1039/D1CY01866C
18. Mathew, S., Ganguly, P., Kumaravel, V., Bartlett, J., Pillai, S. C. (2020). Solar light-induced photocatalytic degradation of pharmaceuticals in wastewater treatment. In *Nano-Materials as Photocatalysts for Degradation of Environmental Pollutants* (pp. 65–78). Elsevier. https://doi.org/10.1016/B978-0-12-818598-8.00004-3
19. Melent'ev, A. B., Kataev, S. S. (2015). Metabolism of designer drugs. Piperazine derivatives. *Sudebno-Meditsinskaya Ekspertiza*, *58*(4), 49–55. https://doi.org/10.17116/sudmed201558349-55
20. Meng, L., Yin, W., Wang, S., Wu, X., Hou, J., Yin, W., Feng, K., Ok, Y. S., Wang, X. (2020). Photocatalytic behavior of biochar-modified carbon nitride with enriched visible-light reactivity. *Chemosphere*, *239*, 1–8. https://doi.org/10.1016/j.chemosphere.2019.124713
21. Pang, Z., Cai, Y., Xiong, W., Xiao, J., Zou, J. (2021). A spectrophotometric method for measuring permanganate index (CODMn) by N,N-diethyl-p-phenylenediamine (DPD). *Chemosphere*, *266*, 1–7. https://doi.org/10.1016/j.chemosphere.2020.128936
22. Pei, S., Zhao, Y., Li, W., Qu, C., Ren, Y., Yang, Y., Liu, J., Wu, C. (2023). Critical impact of pyrolysis temperatures on biochars for peroxymonosulfate activation: Structural characteristics, degradation performance and mechanism. *Chemical Engineering Journal*, *477*. https://doi.org/10.1016/j.cej.2023.147274
23. Prasannamedha, G., Kumar, P. S., Balasubramani, S. R., Parthasarathy, V., Deehen, A. D., Jananie, E., Lokesh, V., Shivani, S., Keerthana, S., Shivani, I., Rangasamy, G. (2025). Engineering properties of hydrochar fabricated from hydrothermal carbonization of lignocellulosic biomass: Practice as adsorbent and catalyst in water treatment. *Journal of Water Process Engineering*, *74*, 1–16. https://doi.org/10.1016/j.jwpe.2025.107739
24. Putri, L. K., Ng, B. J., Er, C. C., Ong, W. J., Chang, W. S., Mohamed, A. R., Chai, S. P. (2020). Insights on the impact of doping levels in oxygen-doped gC3N4 and its effects on photocatalytic activity. *Applied Surface Science*, *504*(October 2019), 144427. https://doi.org/10.1016/j.apsusc.2019.144427
25. Rasheed, H. U., Lv, X., Wei, W., Sam, D. K., Ullah, N., Xie, J., Zhu, W. (2019). Highly efficient photocatalytic degradation of the Tetracycline hydrochloride on the α-Fe2O3@CN composite under the visible light. *Journal of Environmental Chemical Engineering*, *7*(5), 1–10. https://doi.org/10.1016/j.jece.2019.103322
26. Raturandang, R., Wenas, D. R., Mongan, S., Bujung, C. (2022). Analisis spektroskopi ftir untuk karakterisasi kimia fisik fluida mata air panas di kawasan wisata hutan pinus tomohon sulawesi utara. *Jurnal FisTa : Fisika Dan Terapannya*, *3*(1), 28–33.
27. Rodríguez-Chueca, J., Carbajo, J., García-Muñoz, P. (2023). Intensification of photo-assisted advanced oxidation processes for water treatment: A critical review. *Catalysts*, *13*(2), 1–36. https://doi.org/10.3390/catal13020401
28. Rohana, E., Rizqy Prabhata, W. (2023). *Analisis Residu Enrofloksasin Dalam Daging Dan Telur Ayam*. *3*(2), 128.
29. Sciscenko, I., Arques, A., Varga, Z., Bouchonnet, S., Monfort, O., Brigante, M., Mailhot, G. (2021). Significant role of iron on the fate and photodegradation of enrofloxacin. *Chemosphere*, *270*, 1–9. https://doi.org/10.1016/j.chemosphere.2021.129791
30. Shen, X., Chen, J., Lv, S., Sun, X., Dzantiev, B. B., Eremin, S. A., Zherdev, A. V., Xu, J., Sun, Y., Lei, H. (2019). Fluorescence polarization immunoassay for determination of enrofloxacin in pork liver and chicken. *Molecules*, *24*(24), 1–13. https://doi.org/10.3390/molecules24244462
31. Shi, J., Cheng, C., Hu, Y., Liu, M., Guo, L. (2017). One-pot preparation of porous Cr2O3/g-C3N4

composites towards enhanced photocatalytic H2 evolution under visible-light irradiation. *International Journal of Hydrogen Energy*, *42*(7), 4651–4659. https://doi.org/10.1016/j.ijhydene.2016.07.030

32. Sun, S., Wang, Z., Pu, Q., Li, X., Cui, Y., Yang, H., Li, Y. (2024). Identification and mechanistic analysis of toxic degradation products in the advanced oxidation pathways of fluoroquinolone antibiotics. *Toxics*, *12*(3), 1–23. https://doi.org/10.3390/toxics12030203
33. Symochko, L., Mariychuk, R., Demyanyuk, O., Symochko, V. (2019). Enrofloxacin in agroecosystems: Uptake by plants and phytotoxical effect. *2019 International Council on Technologies of Environmental Protection (ICTEP)*, 250–253. https://doi.org/10.1109/ICTEP48662.2019.8968989
34. Tran, H. D., Nguyen, D. Q., Do, P. T., Tran, U. N. P. (2023). Kinetics of photocatalytic degradation of organic compounds: a mini-review and new approach. *RSC Advances*, *13*(25), 16915–16925. https://doi.org/10.1039/D3RA01970E
35. Velo-Gala, I., Farré, M. J., Radjenovic, J., Gernjak, W. (2023). Influence of water matrix components on the UV/chlorine process and its reactions mechanism. *Environmental Research*, *218*, 1–8. https://doi.org/10.1016/j.envres.2022.114945
36. Wang, D., Zhang, M., Xie, Q., Han, S., Xiao, S., Wang, H. (2025). Self-utilization of indigenous materials in plateau areas: Peroxymonosulfate activation by manganese modified barley straw biochar for efficient degradation of enrofloxacin. *Chemical Engineering Research and Design*, *219*, 167–180. https://doi.org/10.1016/j.cherd.2025.06.003
37. Wang, H. Y., Yang, Y., Su, J. Y., Shen, J. L., Gao, C. F., Zhu, Y. C. (2008). Assessment of the impact of insecticides on *Anagrus nilaparvatae* (Pang et Wang) (Hymenoptera: Mymanidae), an egg parasitoid of the rice planthopper, *Nilaparvata lugens* (Hemiptera: Delphacidae). *Crop Protection*, *27*(3), 514–522. https://doi.org/10.1016/j.cropro.2007.08.004
38. Wang, S., Wang, J. (2022). Magnetic 2D/2D oxygen doped g-C3N4/biochar composite to activate peroxymonosulfate for degradation of emerging organic pollutants. *Journal of Hazardous Materials*, *423*. https://doi.org/10.1016/j.jhazmat.2021.127207
39. Wang, T., Zhai, Y., Zhu, Y., Li, C., Zeng, G. (2018). A review of the hydrothermal carbonization of biomass waste for hydrochar formation: Process conditions, fundamentals, and physicochemical properties. In *Renewable and Sustainable Energy Reviews 90*, 223–247. Elsevier Ltd. https://doi.org/10.1016/j.rser.2018.03.071
40. Winingsih, W., Ulfa, M., Suprijana, O. (2016). Penggunaan ftir-atr znse (Fourier transform infra red) untuk penetapan kadar kuersetin dalam teh hitam (*Camellia sinensis* L.). *Indonesian Journal of Pharmaceutical Science and Technology*, *5*(1), 47–53.
41. Wu, S., Lin, Y., Hu, Y. H. (2021). Strategies of tuning catalysts for efficient photodegradation of antibiotics in water environments: a review. *Journal of Materials Chemistry A*, *9*, 2592–2611. https://doi.org/10.1039/D0TA09173A
42. Wu, Y., Wang, H., Sun, Y., Xiao, T., Tu, W., Yuan, X., Zeng, G., Li, S., Chew, J. W. (2018). Photogenerated charge transfer via interfacial internal electric field for significantly improved photocatalysis in direct Z-scheme oxygen-doped carbon nitrogen/CoAl-layered double hydroxide heterojunction. *Applied Catalysis B: Environmental*, *227*, 530–540. https://doi.org/10.1016/j.apcatb.2018.01.069
43. Xiao, Y., Lyu, H., Yang, C., Zhao, B., Wang, L., Tang, J. (2021). Graphitic carbon nitride/biochar composite synthesized by a facile ball-milling method for the adsorption and photocatalytic degradation of enrofloxacin. *Journal of Environmental Sciences*, *103*, 93–107. https://doi.org/10.1016/j.jes.2020.10.006
44. Xie, H., Bei, F., Hou, J., Ai, S. (2018). A highly sensitive dual-signaling assay via inner filter effect between g-C3N4 and gold nanoparticles for organophosphorus pesticides. *Sensors and Actuators B: Chemical*, *255*, 2232–2239. https://doi.org/10.1016/j.snb.2017.09.024
45. Xiong, H.-Q., Bao, H.-R., Long, F., Du, Y.-Y., Qu, J.-Z., Luan, Z.-X., Sun, X.-L. (2024). From lab to nature: Overcoming challenges in applying in-situ photocatalysis to water bodies. *Journal of Environmental Chemical Engineering*, *12*(3), 1–13. https://doi.org/10.1016/j.jece.2024.112656
46. Xu, C., Li, Y., Lu, J., Zhu, X., Li, S., Bai, N., Zhang, J., Zhang, H., Lv, W. (2025a). Efficient biodegradation of enrofloxacin by *Citrobacter* sp. SAASenr-X1: Characteristics, performance, pathways, risk assessment, and practical applications. *Chemical Engineering Journal*, *517*. https://doi.org/10.1016/j.cej.2025.164355
47. Xu, C., Li, Y., Lu, J., Zhu, X., Li, S., Bai, N., Zhang, J., Zhang, H., Lv, W. (2025b). Efficient biodegradation of enrofloxacin by *Citrobacter* sp. SAASenr-X1: Characteristics, performance, pathways, risk assessment, and practical applications. *Chemical Engineering Journal*, *517*. https://doi.org/10.1016/j.cej.2025.164355
48. Xu, H., Zhang, T., Wang, D., Cai, D., Chen, S., Wang, H., Shu, S., Zhu, Y. (2022). Degradation of tetracycline using persulfate activated by a honeycomb structured S-doped g-C3N4/biochar under visible light. *Separation and Purification Technology*, *300*. https://doi.org/10.1016/j.seppur.2022.121833
49. Xu, T., Zou, R., Lei, X., Qi, X., Wu, Q., Yao, W., Xu, Q. (2019). New and stable g-C3N4/HAp composites

as highly efficient photocatalysts for tetracycline fast degradation. *Applied Catalysis B: Environmental*, *245*, 662–671. https://doi.org/10.1016/j.apcatb.2019.01.020

50. Yu, H., Zhang, Z., Zhan, S., Song, S., Sun, S., Zhang, H., Zhang, L., Yu, H. (2023). Study of the kinetics, mechanisms and catalysis activity of photo-electro degradation of organic pollutants via new neural network based methodology. *Applied Catalysis B: Environmental*, *323*, 1–11. https://doi.org/10.1016/j.apcatb.2022.122184
51. Zhang, P., Sun, M., Liang, J., Xiong, Z., Liu, Y., Peng, J., Yuan, Y., Zhang, H., Zhou, P., Lai, B. (2024). pH-modulated oxidation of organic pollutants for water decontamination: A deep insight into reactivity and oxidation pathway. *Journal of Hazardous Materials*, *471*, 1–10. https://doi.org/10.1016/j.jhazmat.2024.134393
52. Zhou, L., Cai, M., Zhang, X., Cui, N., Chen, G., Zou, G. Y. (2019). Key role of hydrochar in heterogeneous photocatalytic degradation of sulfamethoxazole using Ag_3PO_4-based photocatalysts. *RSC Advances*, *9*(61), 35636–35645. https://doi.org/10.1039/c9ra07843f
53. Zulfajri, M., Adlim, M., Andalia, N., Ismulyati, S., Mardhiah, A., Ervilita, R. (2024). Synthesis and characterization of hydrochar by hydrothermal carbonization of pineapple crown waste. *Proc. of International Conference on Multidiciplinary Research*, *7*(1), 84–89. https://doi.org/10.32672/picmr.v7i1.2759